**Proceedings of the ASME 2016 International Design Engineering Technical Conferences &
Computers and Information in Engineering Conference
IDETC/CIE 2016
August 21-24, 2016, Charlotte, North Carolina**

IDETC2016-60168

SHAPE PARAMETERIZATION COMPARISON FOR FULL-FILM LUBRICATION TEXTURE DESIGN

Yong Hoon Lee, Jonathon Schuh, Randy H. Ewoldt, James T. Allison
University of Illinois at Urbana-Champaign, Urbana, IL, 61801
Email: {ylee196,schuh4,ewoldt,jtalliso}@illinois.edu

ABSTRACT

Minimizing energy loss and improving system load capacity and compactness are important objectives for fluid power applications. Recent studies have revealed that a micro-textured surface can reduce friction in full-film lubrication, and an asymmetric textured surface can further improve the performance by reducing friction and increasing normal force simultaneously. As an extension of these previous discoveries, we explore how enhanced texture design can maximize these objectives together. We design the surface texture using a set of distinct parameterizations, ranging from simple to complex (including very general geometries), to improve friction and normal force properties beyond what is possible for limited texture geometries. Here we use a rotational visco-rheometer configuration with a fixed bottom disc, a periodic textured surface, and a rotating top flat disc. The Reynolds equation is formulated in a cylindrical coordinate system and solved using a pseudo-spectral method to model Newtonian fluid flow within the gap between discs. Model assumptions include incompressibility, steady flow, constant viscosity, and a small gap height to texture radius ratio. Multiobjective optimization problems are solved using the epsilon-constraint method with an interior-point algorithm. The trade-off between competing objectives is quantified, revealing important insights. Arbitrary continuous texture geometries are represented using two dimensional cubic spline interpolation. Shifting to more general texture geometries resulted in significant simultaneous improvement in both performance metrics for full-film lubrication texture design. An important qualitative result is that textures resembling a helical blade tend to improve performance for rotating contacts in fluid power systems.

Keywords: Surface texture, shape parameterization, spline interpolation, pseudo-spectral method, full-film lubrication, Reynolds equation, multiobjective optimization, ε-constraint method.

1 INTRODUCTION

Friction is a significant source of energy loss in mechanical components. The influence of surface roughness within lubricated hydrodynamic contacts has been well-studied in the tribology community. Creating micro-dimples at frictional contact interfaces is known to be effective in reducing frictional losses [1]. Furthermore, a recent study proposed a possibility that textured surfaces for sliding hydraulic interfaces can reduce effective friction, improve sealing, and increase the load capacity simultaneously by allowing confined lubricant to shear [2, 3]. However, the roughened or dimpled surfaces in previous studies were restricted to relatively simple shapes, such as randomly roughened surfaces or macroscopic sinusoidal textures [4, 5]. Due to recent manufacturing advancements, such as additive manufacturing and electric/electrochemical micromachining, textures with more general geometries and scalse are realizable for hydrodynamic lubrication surfaces [2, 6, 7].

Film lubrication involves lubricant flow, which is often modeled using the Navier-Stokes equations. Solution of general forms of these equations is computationally expensive, limiting the utility of such models for design studies [3, 8]. In hydrodynamic lubrication, however, the distance between sliding surfaces is much smaller than other length scales in the system; this allows the governing equations for flow to be simplified to the Reynolds equation, which is more favorable for computation [9]. In a recent study, the Reynolds equation was solved for the full-
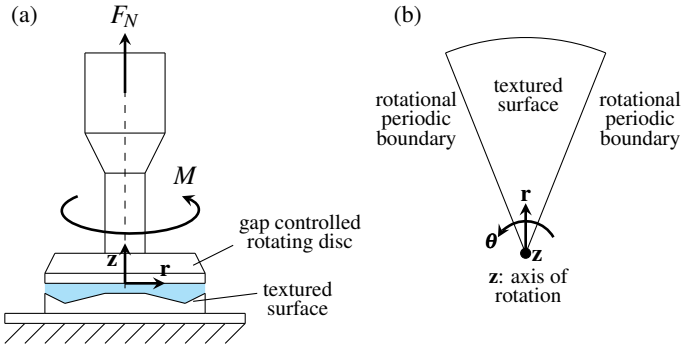
FIGURE 1: Textured surface design problem setup adapted from experiments conducted by Schuh and Ewoldt [12]. The asymmetric dimpled textures used in the previous study are replaced here with arbitrary continuous texture shapes. (a) Front view of experimental setup, (b) top view of one sector of textured surface.

FIGURE 2: The ε-constraint method converts a multiobjective optimization problem to multiple single objective optimization problems. For each scalarized problem, one objective is minimized while satisfying bound constraints on the other objectives.

film lubrication problem with circular dimples using the pseudo-spectral method. This numerical method exhibits exponential convergence with respect to polynomial basis functions order, and was demonstrated to be computationally efficient [10].

Here we are building upon this pseudo-spectral solution method for the Reynolds equation to explore a much wider range of surface texture designs with the primary objective of friction reduction. Arbitrary continuous texture shapes are optimized using effective parameterization techniques. Important existing options for describing curved shape designs include basis vectors, domain elements, polynomial functions, splines, and analytical approaches. These methods are often used in aeronautical system design (e.g., airfoil shape optimization) [11]. The specific parameterization used in this study involves spline functions defined in two orthogonal directions to represent arbitrary texture shapes in three dimensional space.

2 PROBLEM DESCRIPTION

The objective of the design problem in this study is to maximize the film lubrication efficiency and effectiveness by designing the shape of the textured surface using systematic methods. The experimental setup in Schuh and Ewoldt [12] revealed that asymmetric dimpled surface textures decrease frictional loss. Figure 1(a) illustrates the problem setup used for the previous experimental research. Based upon this configuration, we perform a more comprehensive study here enabled by more flexible texture surface design representation and exploration. A pair of gap-controlled discs are aligned axially, and are separated by a Newtonian fluid. The rotating upper disc is flat, while the stationary bottom disc is textured. All points of the surface in the design domain—illustrated in Fig. 1(b)—are defined using a moderate-dimension spline representation. The design domain is a sector of the bottom disk instead of the entire disk. Simulation results are equivalent to the behavior of a full disc with repeated sec-
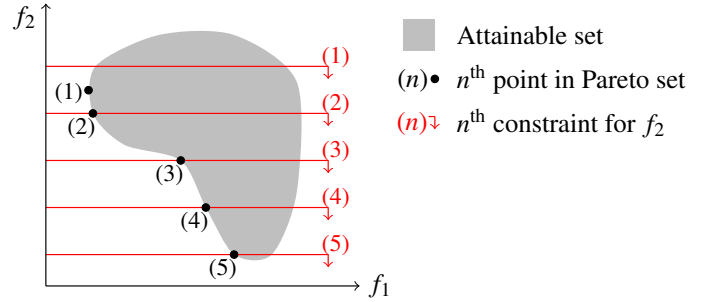
tors. This simplification reduces computational expense, and is assumed to be reasonable due to the rotational nature of the setup. The sector surface design is assumed to be periodic, i.e., the texture repeats and the boundaries of each sector match to preserve texture continuity.

3 OPTIMIZATION METHOD

3.1 Multiobjective Optimization

Multiobjective optimization involves minimization or maximization of a set of multiple conflicting objective functions. The solution of such a problem is a set of non-dominated (Pareto-optimal) solutions, as opposed to a single optimum point as with single objective optimization. A design point is non-dominated if one objective cannot be improved without degrading at least one other objective [13].

Two primary classes of methods are used to solve multiobjective optimization problems: population-based or scalarization-based methods. Population-based methods, such as multiobjective genetic algorithms (MOGAs), solve the optimization problem once and generate a set of solutions that form the Pareto set (approximately). These methods often improve the probability of finding global instead of local optima, but may be computationally expensive due to the large number of function evaluations typically required [14].

The second class of methods convert a single multiobjective problem into a set of 'scalarized' single objective problems. These scalarization-based methods are often used in design optimization studies due to their computational efficiency and simplicity [15]. The weighted-sum method is the simplest scalarization approach, but cannot identify non-dominated solutions in non-convex regions of a Pareto front. In addition, resulting non-dominated points are often clustered instead of uniformly distributed across the Pareto surface. These limitations can be overcome through other more sophisticated scalarization approaches, such as the ε-constraint method [16], which is illustrated in Fig. 2 and described in Section 3.3.

3.2 Multiobjective Formulation

The conflicting objectives of the full-film lubrication problem here are to 1) minimize the normalized apparent viscosity, and 2) to maximize the normal force. Friction is a significant source of energy loss for systems involving lubricated hydrodynamic contacts. Friction can be reduced by increasing the gap between the sliding contact surfaces. Increasing this gap, however, degrades load capacity and sealing performance.

Fluid and pressure loss due to poor sealing are very undesirable outcomes for fluid power systems. Improved sealing requires increased normal force, but increased normal force normally increases frictional losses (e.g., fluid squeeze-out, higher viscosity, etc.) [17]. These two objective functions therefore conflict, and the solution to this multi-objective design problem will be a set of non-dominated points that quantify trade-off options. Adding certain types of textures to the full-film lubrication problem was found in previous studies to simultaneously improve both of these objective functions. In other words, transitioning to more effective texture classes shifts the Pareto surface toward more desirable objective function values. These previous studies were limited to very simple uniform dimpled textures. Here we aim to shift the attainable Pareto set even more by considering more general texture designs. We also aim to gain fundamental insights about how best to design surface textures for full-film lubrication applications.

The multiobjective problem formulation used here is:

$$\min_{\mathbf{x}} \left\{ \frac{\eta_a(\mathbf{x})}{\eta_0}, -F_N(\mathbf{x}) \right\} \tag{1a}$$

$$\text{subject to } \mathbf{x}_{\min} \leq \mathbf{x} \leq \mathbf{x}_{\max}, \tag{1b}$$

$$h_{\min} \leq h_{ij}(\mathbf{x}) \leq h_{\max}, \forall\{i,j\} \in \mathfrak{D}, \tag{1c}$$

where $\mathbf{x}$ is a vector of design variables that represents texture geometry (e.g., spline, etc.). In this study geometric parameterizations implicitly satisfy the periodic boundary conditions for the surface shape. For a given value of $\mathbf{x}$, the resulting geometric surface description is then used to determine high-resolution surface height values: $h_{ij}(\mathbf{x}), \forall\{i,j\} \in \mathfrak{D}$. The height values $h_{ij}(\cdot)$ quantify the surface shape at mesh points needed for the pseudospectral method, and $\mathfrak{D}$ is the set of indices for all mesh points in the design domain. The objective functions ultimately depend on $\mathbf{x}$. The height values, obtained from $\mathbf{x}$, are used within the simulation to obtain intermediate quantities needed to compute the objective function values. The simulation solves for the pressure distribution $p(r,\theta)$ that is a function of radial (r) and angular (θ) positions. The first objective function, normalized apparent viscosity ($\eta_a(\mathbf{x})/\eta_0$), is calculated by a ratio of apparent viscosity ($\eta_a(\mathbf{x})$, depends on design) to actual fluid viscosity (η_0, fixed, depends on fluid selection). The apparent viscosity is defined as shear stress divided by strain rate. For the rotating disc configuration, apparent viscosity can be written as a function of disk

torque (M) as shown in Eqn. (2a).

$$\eta_a = \eta_a(M) = \frac{2h_0}{\pi R_o^4} \frac{M}{\Omega} \tag{2a}$$

$$F_N = F_N(p) = N_\phi \int_{-\varphi/2}^{\varphi/2} \int_{R_i}^{R_o} p\, r\, dr\, d\theta \tag{2b}$$

$$\text{where,} \quad \tau_{\theta z}|_{z=0} = -\frac{1}{2}\frac{1}{r}\frac{\partial p}{\partial \theta} h - \eta_0 \frac{r\Omega}{h} \tag{2c}$$

$$\text{and } M = N_\phi \int_{-\varphi/2}^{\varphi/2} \int_{R_i}^{R_o} \tau_{\theta z}|_{z=0}\, r^2\, dr\, d\theta \tag{2d}$$

R_o is the outer radius of textured disc; h_0 is a controlled minimum gap height between the fixed and rotating discs; Ω is the rotating disk angular velocity. Equation (2d) defines how disk torque is calculated, which requires evaluation of the θ-direction (tangential) shear stress ($\tau_{\theta z}(r,\theta)$, where z is the vertical coordinate) at the rotating surface across the complete domain. The shear stress calculation, defined in Eqn. (2c), requires knowledge of the pressure field ($p(r,\theta)$) across the entire computational domain. The pressure field is computed by solving the Reynolds equation given in Eqn. (4). The second objective function, the negative normal force ($-F_N$), is calculated by integrating pressure over the domain, and then multiplying this value by the total number of disk sectors (N_ϕ) as shown in Eqn. (2b).

3.3 ε-constraint method

The ε-constraint method is a type of scalarization technique for multiobjective optimization. A multiobjective problem is transformed to a single objective problem by retaining just one of the original objective functions, and the remaining objective functions are converted to constraints that bound these other objective function values [16]. Figure 2 illustrates how the ε-constraint method minimizes the first objective function ($f_1(\cdot)$), while a constraint prevents the second objective function ($f_2(\cdot)$) from exceeding a bound denoted by red horizontal lines. This procedure is repeated, each time with a different bound on $f_2(\cdot)$. In the example shown in Fig. 2 the optimization problem is solved five times to generate five Pareto-optimal solutions. This strategy supports the use of existing single-objective optimization algorithms in solving multiobjective problems, including the ability to resolve non-convex portions of the Pareto surface, and to generate well-distributed Pareto-optimal points. The multiobjective formulation in Prob. (1) can be reformulated for ε-constraint solution as follows:

$$\min_{\mathbf{x}} \frac{\eta_a(\mathbf{x})}{\eta_0} \tag{3a}$$

$$\text{subject to } -F_N \leq \varepsilon_k \tag{3b}$$

$$\mathbf{x}_{\min} \leq \mathbf{x} \leq \mathbf{x}_{\max} \tag{3c}$$

$$h_{\min} \leq h_{ij}(\mathbf{x}) \leq h_{\max}, \forall\{i,j\} \in \mathfrak{D} \tag{3d}$$

$$\forall k \in \{1, 2, \ldots, n_p\}, \tag{3e}$$

where n_p is the number of Pareto-optimal points to solve for. One possible strategy is to increment ε_i uniformly, i.e., $\varepsilon_{i+1} = \varepsilon_i + \delta$, where $\varepsilon_1 = (-F_N)_{\min}$ and $\delta = ((-F_N)_{\max} - (-F_N)_{\min})/(n_p - 1)$.

4 FLOW SIMULATION METHOD

The Reynolds equation given in Eqn. (4) below can be derived from the mass and momentum conservation equations for an incompressible Newtonian fluid, with boundary conditions given in Eqn. (5), and assumptions (1)–(5) listed below [10]. The resulting partial differential equation (PDE) in Eqn. (4) is discretized using the pseudo-spectral method, which is a variation of the weighted residual technique (WRT), where the PDE is solved in its variational form [18]. The resulting integrals for the variational form of the PDE are solved using Gauss-Lobatto-Legendre (GLL) quadrature, where the function evaluations occur at the GLL points and the quadrature weights are chosen optimally such that the integral is exact for polynomials of degree $2N - 1$, where N is the number of evaluation points [10, 18, 19].

$$\frac{1}{r}\left(rh^3\frac{\partial p}{\partial r}\right) + \frac{1}{r}\frac{\partial}{\partial \theta}\left(\frac{h^3}{r}\frac{\partial p}{\partial \theta}\right) = 6\eta\Omega\frac{\partial h}{\partial \theta} \qquad (4)$$

$$v_\theta = r\Omega \text{ and } v_r = v_z = 0 \qquad \text{at } z = 0 \qquad (5a)$$
$$v_\theta = v_r = v_z = 0 \qquad \text{at } z = h \qquad (5b)$$

Assumptions:

(1) Steady state conditions with fixed angular velocity: $\Omega = 10$ [rad/s]
(2) Constant viscosity: $\eta_0 = 1.4$ [Pa·s]
(3) Inertial terms are negligible
(4) $p = p(r, \theta)$
(5) $h \ll R$, where R is the reference radius

5 SURFACE PARAMETERIZATION

In previous related work surface textures have been described using very simple parameterizations. For example, one strategy assumes that surface texture features consist only of cylindrical dimples, either with flat or angled lower surfaces, and are parameterized using dimple diameter, depth, lower surface angle [3, 12]. A core objective of the present study is to perform design exploration of much more general texture designs as a means to gain greater insight into surface texture design for fluid power systems. One strategy is to simply use h_{ij}, the surface height at mesh (GLL) points, as the surface design description. While this provides high accuracy and a high-resolution design description, it results in a large-dimension nonlinear optimization problem. Current implementations of the optimization problem solution require treating the simulation (i.e., in this study, lubricant flow computation) as a black box, necessitating finite difference calculations. While ongoing work is focused on investigating alternative implementations that leverage problem structure, such
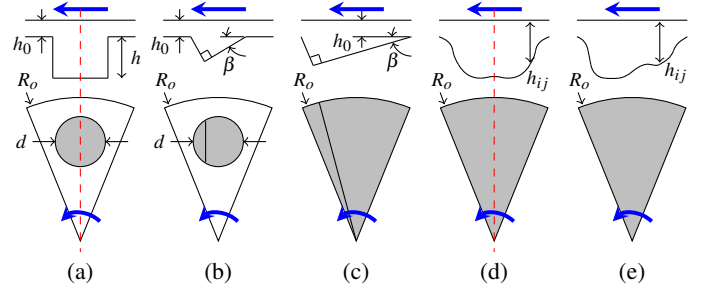

FIGURE 3: Alternative texture shape design representations. A cross-sectional view of each representation is shown in the top row, while a top view of each textured sector is shown in bottom row. The gray area denotes the textured region (non-gray regions indicate unchanged flat surfaces). The top flat plates are rotating in the direction of thick blue arrow, while the bottom textured surfaces are fixed. (a) Symmetric cylindrical texture, (b) asymmetric cylindrical texture, (c) asymmetric planar texture spanning full disc area, (d) arbitrary continuous texture with symmetry constraint, (e) arbitrary continuous texture.
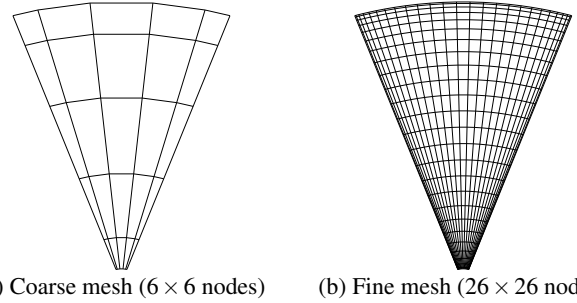

(a) Coarse mesh (6×6 nodes)   (b) Fine mesh (26×26 nodes)

FIGURE 4: The mesh for a reduced-dimension cubic spline texture shape design representation is shown on the left. This design mesh is much more coarse than the mesh on the right that is required for accurate simulation. The surface geometry defined by the cubic spline is interpolated to determine all the height values at the fine mesh points required for simulation.

a large-dimension design representation is impractical for the present study. In previous work it was determined for this system configuration the coarsest practical mesh involves 26×26 GLL points [10]. Using h_{ij} directly, accounting for periodic boundary constraints, would therefore require $26 \times (26 - 1) = 650$ optimization variables. A reduced-dimension design representation is needed. For visual comparison, the simple angled cylindrical dimple textures from previous work are illustrated in Figs. 3(a–b). The aim here is to support exploration of more general texture design shapes, as shown in Figs. 3(c–e), with reduced dimension, and to evaluate performance improvements available through these more general texture designs. The simplified cylindrical texture parameterization is reviewed first, followed by a description of a more general two-dimensional spline representation.

TABLE 1: Cylindrical textured surface parameters

Item			symmetric	asymmetric
Disc radius	R_o	[mm]	20	20
Location of texture	R_c	[mm]	14.3	14.3
Sector division	N_ϕ	[#]	10	10
Nominal gap height	h_0	[mm]	0.269	0.269
Radius of texture	R_t	[mm]	$1 \le x_1 \le 4$	$1 \le x_1 \le 4$
Depth of texture	h	[mm]	$0 \le x_2 \le 2.5$	-
Angle of texture	β	[°]	0	$0 \le x_2 \le 20$

TABLE 2: Spline interpolated textured surface parameters

Item			symmetric	asymmetric
Disc radius	R_o	[mm]	20	20
Sector division	N_ϕ	[#]	10	10
Min. gap height	h_0	[mm]	0.269	0.269
Depth of texture	h_{ij}	[mm]	$h_0 \le x_{ij} \le 1.5$	$h_0 \le x_{ij} \le 1.5$
Max. local slope	ϕ	[°]	30	30

5.1 Cylindrical textures

The previous experimental setup involved a single cylindrical dimple with fixed location in each sector. The asymmetric texture angle was varied in these previous studies to gain an initial understanding of this behavior [3, 12]. Here we build upon these initial studies by optimizing this dimpled texture design. The complete set of cylindrical dimple parameters is listed in Table 1. Three of these parameters, radius, depth, and angle, are selected as design variables (x_1, x_2, x_3). Geometric configurations of these textures are illustrated in Figs. 3(a–b) along with the shape parameters.

5.2 Inclined plane spanning full disc sector

In the full factorial design results of cylindrical texture shown in Fig. 5, both objectives are enhanced monotonically when the texture area is increased by magnifying the radius of the cylindrical texture. With this observation, we can predict that if the texture area spans the full sector area, it may be possible to shift the Pareto front closer to the origin. To demonstrate the effect of expanded texture area, a new geometric parameterization is defined where the entire sector is an inclined plane tilted at angle β, as shown in in Fig. 3(c). Note that this geometry is continuous, but non-smooth.

5.3 Other low-order design representations

Polynomial texture: A few additional low-order design representations were investigated in addition to the cylindrical and inclined plane texture parameterizations. First, a uni-modal polynomial function was used to generate the height profile by spec-

ifying peak function height location. Height at both periodic sides and the inner/outer boundaries was fixed to the nominal gap height (h_0). Numerical experiments indicated that this class of textures performed poorly, possibly because large local slopes could not be achieved. Detailed results for this case are omitted for brevity.

Radial-basis function texture: Radial-basis functions (RBFs) are used widely in approximating or interpolating functions. RBFs were tested as a texture geometry representation where the height and location of a number of thin-spline RBFs were used as design variables. Several challenges were discovered. Changing texture design in significant ways requires changing the number of RBFs used, which cannot be done during optimization solution using continuous algorithms. In addition, the number of parameters required is large relative to the range of texture geometries that are accessible. Each RBF requires at least three parameters. RBFs do not provide a low-dimension representation, and do not support efficient design space exploration for this problem compared to the spline representation discussed next. Detailed results for this case are again omitted for brevity.

5.4 Two-dimensional cubic spline interpolation

Here we introduce a low-dimension texture design representation that supports description of arbitrary continuous geometries. This provides enhanced design flexibility and the possibility of capitalizing on new mechanisms for improving fluid system performance. To describe the full-sector texture design using a limited number of design variables, the height profile is specified at nodes of the coarse mesh shown in Fig. 4(a). As a manufacturability constraint, the inclination angle between course mesh nodes is limited to a maximum of 30°. After specifying a low resolution height profile, the two-dimensional spline representation is used to map this profile onto the fine computational mesh shown in Fig. 4(b). This allows the surface texture design to be specified using a limited number of design variables, while still supporting high-resolution simulation. A symmetry constraint can be imposed. Symmetric designs are investigated first, as shown in Fig. 3(d), followed by studies of asymmetric designs, shown in Fig. 3(e), that further improve fluid system performance.

6 RESULTS AND DISCUSSION

6.1 Cylindrical textures

A full factorial set of cylindrical texture designs, both in symmetric and asymmetric configurations, was generated and evaluated to provide insight into how design variables influence objective functions, and to assess trade-offs. Texture radius (R_t) and depth (h) are the design variables used for the symmetric cylindrical texture study, and texture radius (R_t) and angle (β) are the design variables used for the asymmetric cylindrical texture study. Figure 5 illustrates the contours of the two objective functions for
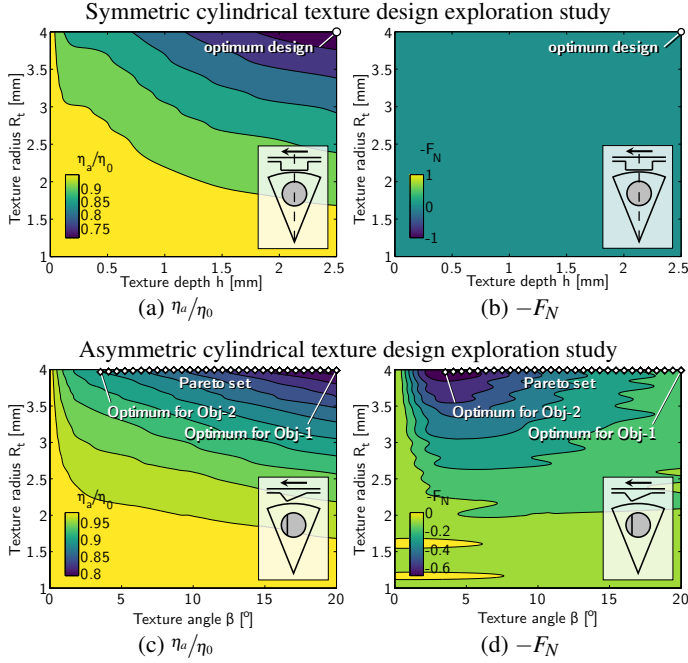
FIGURE 5: Objective function contours based on comprehensive sampling of the cylindrical texture design (symmetric and asymmetric textures). Trade-offs are apparent, and the Pareto sets are illustrated in the figures. Asymmetry improves performance capability, especially in terms of normal force.
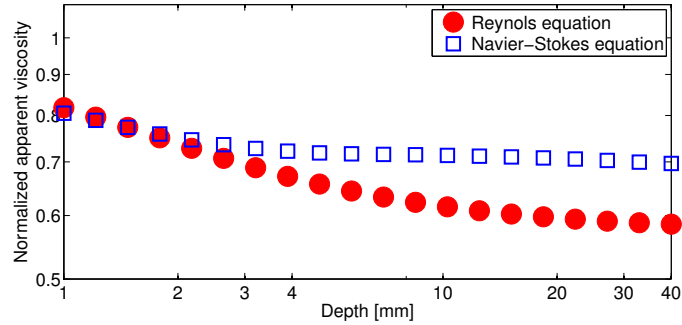

FIGURE 6: Comparison of the Reynolds equation and the Navier-Stokes equation solutions in terms of the normalized apparent viscosity for the symmetric cylindrical textures as a function of depth.

both cases. Figures 5(a–b) correspond to the symmetric texture, and Figs. 5(c–d) correspond to the asymmetric texture.

The minimum of the first objective, normalized apparent viscosity, for the symmetric texture is 0.7129, while the normal force is maintained at 0 N. Objective function values range more widely for the asymmetric configuration: normalized apparent viscosity ranges from 0.7942 to 0.9020, and the negative normal force ranges from -0.1623 to -0.6924. Asymmetry is required to improve normal force. This trade-off is illustrated in Fig. 10(a).
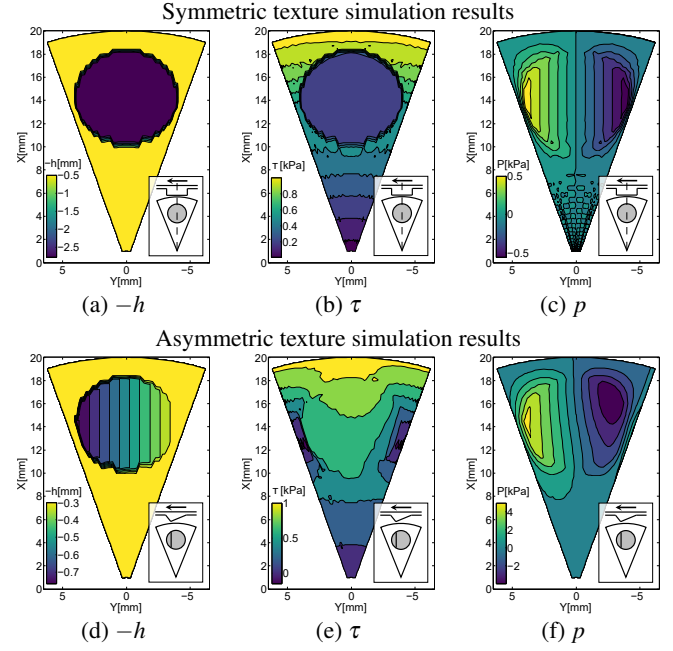

FIGURE 7: Geometry, shear stress, and pressure fields of optimized cylindrical texture designs in symmetric and asymmetric configurations.

Design variable bounds are chosen such that the Reynolds equation simulation results agree with results based on the full Navier-Stokes equation. Figure 6 shows both Reynolds equation and Navier-Stokes equation solutions in terms of normalized apparent viscosity for the symmetric cylindrical texture problem. When the texture depth becomes deeper than 2mm, the solution of Reynolds equation deviates from the solution of full Navier-Stokes equation. Due to this limitation in Reynolds equation model, the depth variable should be constrained to preserve accuracy. Furthermore, as can be seen for greater depth values in Fig. 6, normalized apparent viscosity plateaus beyond a certain depth (note that the plot is log-scale). This means that the frictional performance cannot be enhanced any more through increases in depth beyond a certain value.

For both symmetric and asymmetric textures, the first objective function (normalized apparent viscosity) has monotonic dependence on texture depth and radius as shown in Figs. 5(a, c) (the objective decreases with increasing depth and radius). In the asymmetric configuration study the angle was varied between 0-20°. Within this range, increasing the angle corresponds to increased average texture depth, and increased lubricant volume. This observation, along with the results presented here, indicate that the total volume removed for a texture is important for reducing friction.

The behavior of the second objective function (negative normal force) is different for the symmetric and asymmetric configurations. Symmetric cylindrical design variables do not influence normal force because geometric symmetry in the slid-
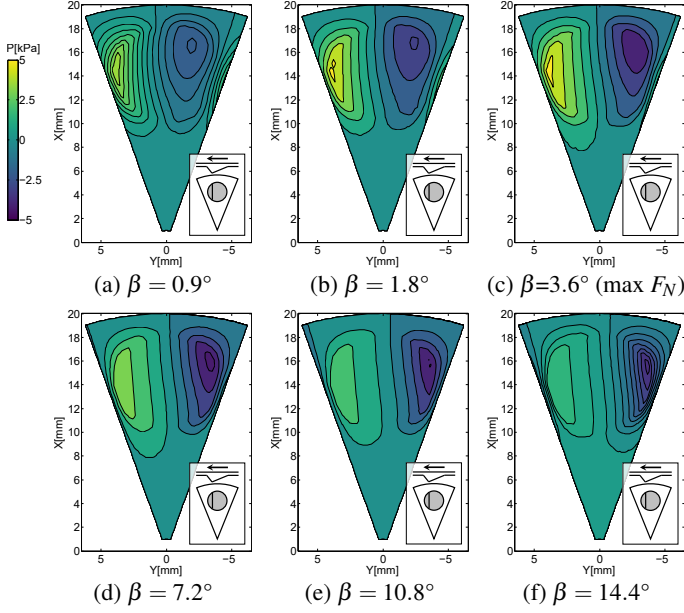
(a) $\beta = 0.9°$ (b) $\beta = 1.8°$ (c) $\beta = 3.6°$ (max F_N)

(d) $\beta = 7.2°$ (e) $\beta = 10.8°$ (f) $\beta = 14.4°$

FIGURE 8: Contours of pressure field for asymmetric cylindrical textures with various angles.

ing direction countervails negative and positive pressure distributions through the expanding-contracting channel gap height. This matches the results reported in previous experimental and theoretical studies that measurable normal forces were not detected in symmetric cylindrical surface textures [9, 12].

The second objective function varies widely when changing the asymmetric configuration design variables. Figure 5(d) shows that the normal force depends on both the texture angle β and the radius R_t. In particular, the best normal force value occurred at a specific texture angle value, $\beta = 3.601°$, with the texture radius R_t at the upper bound, 4.0mm. Moving away from this point improves normalized apparent viscosity, but degrades normal force. The result of this optimization study, therefore, is a set of non-dominated designs that express the trade-off between the two objective functions. Figure 10(a) shows the optimization results for both the symmetric and asymmetric configurations in the objective function space. The red line in this plot denotes the Pareto set for the asymmetric texture design problem. We can improve normal force through asymmetric textures, but at the cost of degraded apparent viscosity.

Geometry, shear stress, and pressure distribution in the flow fields of symmetric and asymmetric cylindrical textures are shown in Fig. 7. The asymmetric texture simulation results are based on a Pareto-optimal design, shown in Fig. 7(d), that maximizes normal force. The symmetric texture simulation results are based on the design shown in Fig. 7(a). The pressure field results in Fig. 7(c) shows that the pressure is counterbalanced between each side of the vertical line of symmetry. Thus, the overall pressure acting in the direction normal to sliding is canceled,
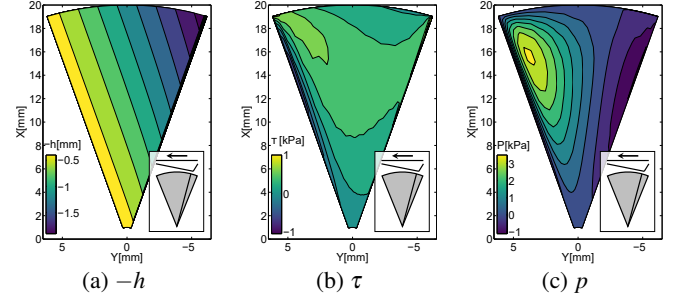

(a) $-h$ (b) τ (c) p

FIGURE 9: Geometry, shear stress, and pressure field of the surface texture with inclined plane spanning full sector area.

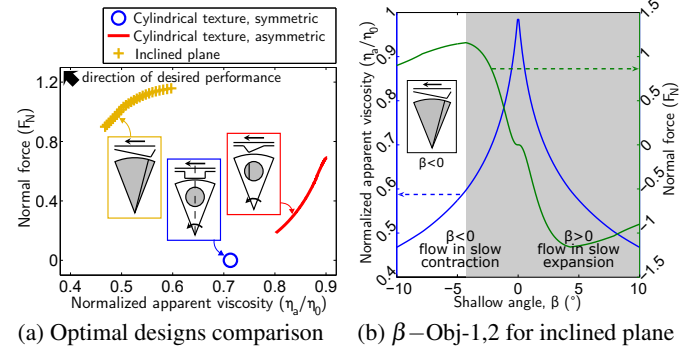(a) Optimal designs comparison (b) β−Obj-1,2 for inclined plane

FIGURE 10: Optimal designs for the cylindrical design exploration and the inclined plane spanning full sector area studies. The solid red line in (a) is the Pareto set for the cylindrical texture identified by interpolating the contours of Figs. 5(c–d). In (b), design and two objectives are plotted together.

resulting in no normal force. This numerical result explains why design variables in symmetrical texture have no effect on the normal force for the symmetric texture case, as shown in Fig. 5(b).

For the asymmetric configuration, the pressure distribution is not balanced and can produce a net normal force. Here the positive overall pressure generates positive normal force. Figure 8 shows how pressure distribution changes with changes in angle. At the angle of maximum normal force ($\beta = 3.6°$), the net pressure difference is at its maximum. The maximum normal force increases with β up to $\beta = 3.6°$, but then decreases with angle beyond $\beta = 3.6°$. The interface between positive and negative pressure consistently moves from left to right with increasing angle. This is because when the angle of asymmetry is greater than $45°$, the resulting surface texture is geometrically similar to a texture with an angle of $90° - \beta$ with the flow in the opposite direction, and it has been shown previously that when the direction of motion changes for asymmetric surface textures, the sign of the normal force also changes [10, 12].

7

6.2 Inclined plane spanning full sector area

By expanding the inclined region of the texture to the entore sector, both objectives can be improved simultaneously. In Fig. 10(a), it is clear that normalized apparent viscosity is reduced significantly when shifting to the full inclined plane geometry. Since this design representation has only a single design variable, (β), it is possible to visualize the response of both objectives with respect to β as shown Fig. 10(b). This plot shows a clear conflict between the two objective functions.

6.3 Arbitrary continuous texture designs

The study is now extended to arbitrary continuous surface elevation changes parameterized using spline interpolation. Objectives of this investigation include understanding how to improve fluid power system performance further through more sophisticated texture designs, and what physical mechanisms make any improvements possible.

Using the coarse mesh described above, designs are represented using a $6 \times (6-1)$ matrix of surface elevation values, accounting for periodic boundary constraints. The resulting design representation dimension is 30. Figure 11 shows the geometry, shear stress, and pressure field for the optimal design with symmetry and inclined angle constraints. As with the symmetric cylindrical texture result, the pressure distribution is balanced and the normal force is zero. As before, the problem reduces to a single objective function problem due to symmetry and insensi-
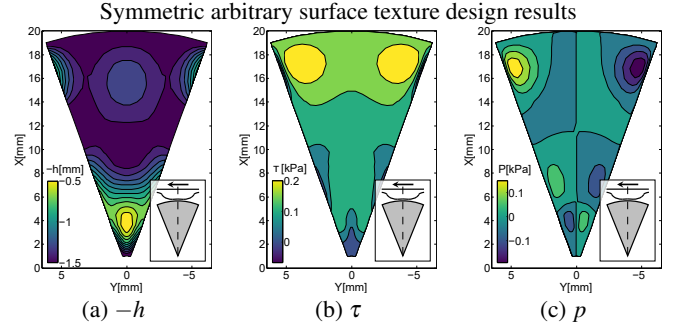

Symmetric arbitrary surface texture design results

(a) $-h$ (b) τ (c) p

FIGURE 11: Geometry, shear stress, and pressure field of the optimized surface texture with spline design representation in a symmetric configuration.

tivity of normal force to texture design. The minimum value for the remaining objective function (normalized apparent viscosity) is 0.2045, whereas the minimum value achieved with cylindrical texture with symmetric configuration is 0.7129. Thus, allowing more general surface texture designs leads to significant performance improvement.

When the symmetry constraint is removed, the sliding surface textures can generate non-zero normal forces as with the asymmetric cylindrical texture designs. Figure 12 shows asymmetric texture geometry and the corresponding pressure fields for six different Pareto-optimal designs. Designs are displayed
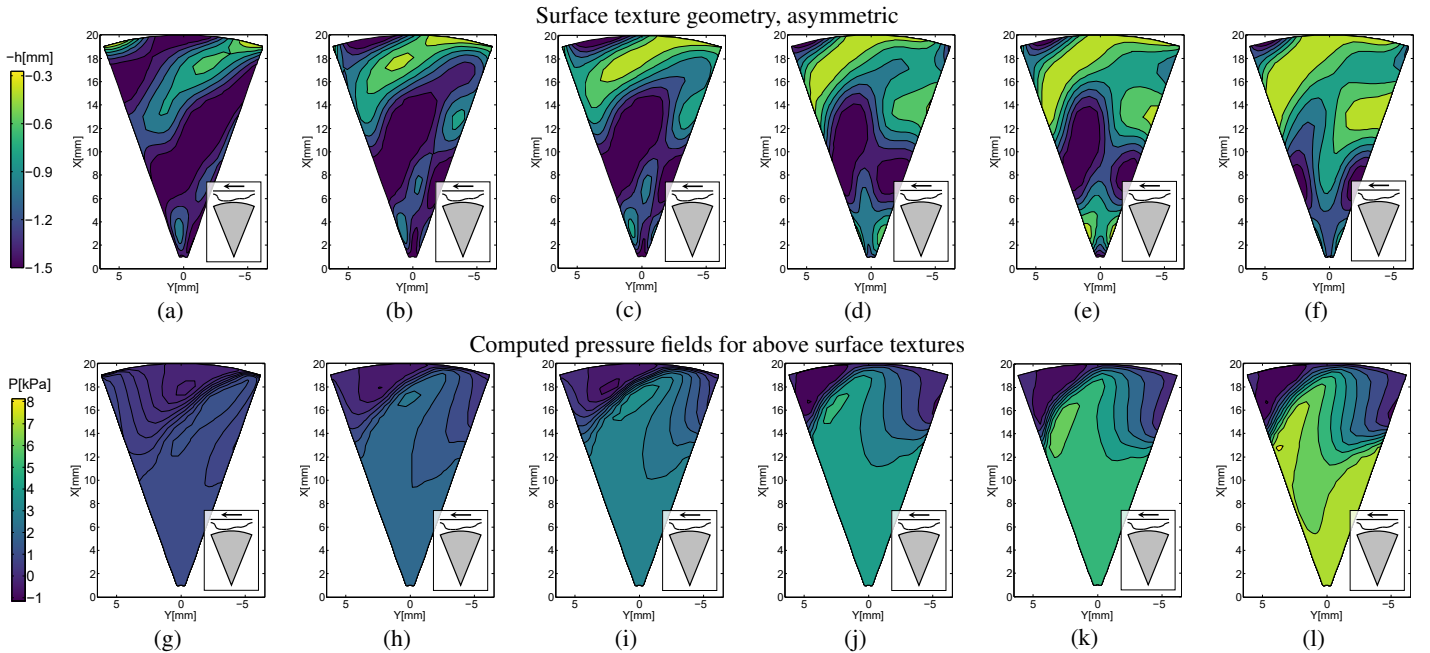

Surface texture geometry, asymmetric

(a)   (b)   (c)   (d)   (e)   (f)

Computed pressure fields for above surface textures

(g)   (h)   (i)   (j)   (k)   (l)

FIGURE 12: Geometry and pressure field of optimized surface texture with spline design representation. Asymmetry is permitted. Six designs are uniformly sampled from 27 designs in the Pareto set to illustrate trends. (a)-(f) are geometric texture profile level sets, and (g)-(l) are pressure field level sets.

8

in order of increasing normalized apparent viscosity value (and decreasing negative normal force). The designs shown in Fig. 12 are sampled uniformly from the Pareto set obtained by solving Prob. (3). The corresponding Pareto set is shown as blue squares (ref. case) in Fig. 13, which is observed to be non-convex in the objective-function space. Using an approach such as the ε-constraint method was essential for resolving non-convex portions of the Pareto set.

In some portions of the design domain, the texture slope has significant impact on results. It may be helpful (e.g., for manufacturability) to add constraints to limit texture slope in further design studies. This could be implemented approximately using linear constraints on design variables. With the 30-variable spline representation, this slope constraint strategy requires $2 \times (6-1)^2 = 50$ linear constraints. All of spline interpolated studies presented here use these linear constraints to limit the inclined angle of texture profile.

The geometric result shown in Figs. 12(a–f) converged to a shape that is similar to a helical blade. Flow velocity in the shear direction is higher toward the outer edge (large radial positions). The helical blade-like texture profile has a portion colored in yellow (Figs. 12(a–f)) that acts as a converging channel directing flow radially inward. This increases pressure near the disk center and generates a positive net normal force. This mechanism helps explain how the asymmetric helical blade-like surface design can help increase normal force. The increased pressure near the disc center will also help reduce leakage, an important practical consideration for fluid power systems. This increased pressure at the center helps support axial work loads and load applied on the sealing components, while the low hydraulic pressure near the outer rim of the discs helps to contain the fluid within the gap between sliding discs.

6.4 Comparison of optimal designs

Pareto-optimal designs shown in Fig. 13 show how the objective functions can be improved significantly by transitioning from simple dimpled textures to arbitrary continuous texture geometries. Note that the vertical axis is F_N as opposed to $-F_N$, so points closer to the upper left are more desirable. Only normalized apparent viscosity (η_a/η_0) changes in the symmetric cases. The spline representation enables identification of a design where the apparent viscosity is reduced to 20.45% of that in the cylindrical dimple texture, i.e., 79.55% of frictional losses is eliminated when using symmetric spline representations. For the asymmetric case, switching from dimpled cylindrical to arbitrary spline-based textures shifts the Pareto sets significantly toward the upper left, indicating roughly an order of magnitude performance improvement. Enhanced normal force generation is observed as more spline control points are added as design variables (increasing texture design resolution). In the region of nearly zero normal force, however, increasing the number of
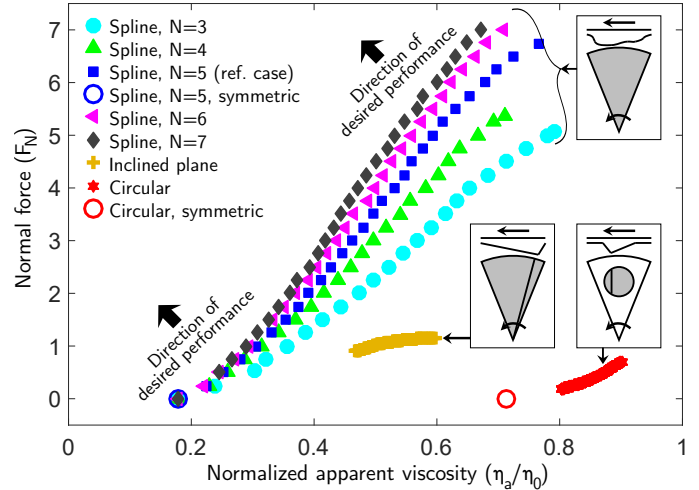

FIGURE 13: Comparison of optimal designs in the objective function space for all design studies presented in this article. Performance indices are improved significantly by increasing design flexibility via the texture surface representation.
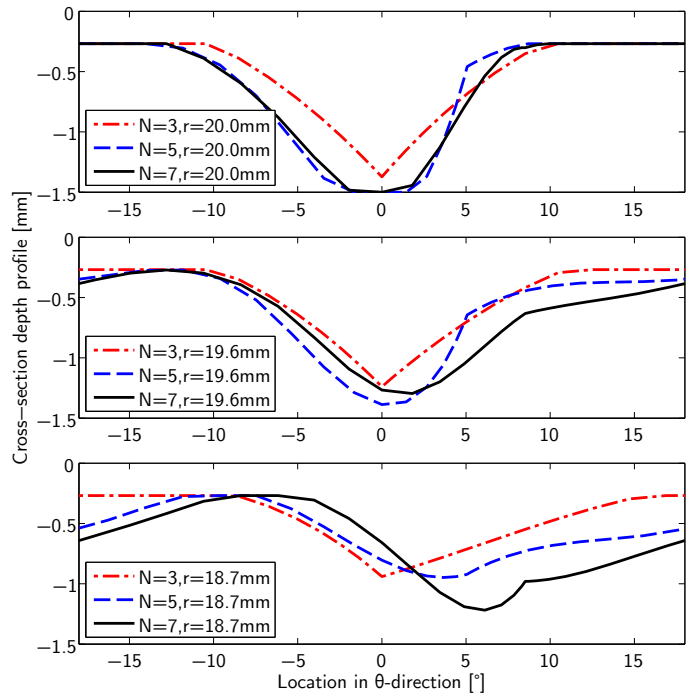

FIGURE 14: Comparison of depth profiles: cross-sectional view of optimal designs, spline design representation cases with $N = 3, 5, 7$, and $F_N = 5$[N].

spline control points (N) does not provide meaningful improvement in reducing normalized apparent viscosity.

Figure 14 illustrates comparisons of optimal cross-sectional depth profiles for spline-based designs across a range of tex-

TABLE 3: Comparison of average computation cost per single scalarized optimization problem and system performance obtained from ε-constraint method and interior-point (IP) algorithm

Order of design mesh (number of variables)		N=3 (4×3)	N=4 (5×4)	N=5 (6×5)	N=6 (7×6)	N=7 (8×7)
Computation time per single IP run [minute]		2.2	3.6	7.8	12.0	18.8
F_N [N]	at $\eta_a/\eta_0 = 0.3$	0.48	0.87	0.95	1.08	1.15
	at $\eta_a/\eta_0 = 0.5$	2.27	3.04	3.57	4.03	4.49
	at $\eta_a/\eta_0 = 0.7$	4.39	5.32	6.29	6.95	7.28
$\dfrac{\eta_a}{\eta_0}$	at $F_N = 1$	0.36	0.31	0.30	0.29	0.29
	at $F_N = 3$	0.57	0.50	0.46	0.44	0.42
	at $F_N = 5$	0.78	0.67	0.59	0.56	0.53

ture resolutions ($N = 3, 5, 7$) for three different radial positions. Among solutions in the Pareto set, the optimal design point generating the normal force of $F_N = 5$[N] is chosen for this comparison. At all three resolutions, the same trend is observed. Namely, texture profiles consist of asymmetric expansion-contraction channels. In addition, these periodic asymmetric profiles shift to the right with decreasing radial position, resulting in helical texture geometries. While low-dimension spline representations ($N = 3$) produce texture geometries that can capitalize on the physical effects discussed above, increasing N results in smoother designs and improved performance. Higher-resolution representations, however, increase computational expense (discussed next).

6.5 Computational expense comparison

All problems were solved using dual Intel® Xeon® X5650 CPUs with a total 12 physical cores. Gradient evaluation within the interior-point algorithm is computed in parallel to utilize all CPU cores. All cases converged to solutions with a function value tolerance of 10^{-16}. A summary of average computation time for single scalarized problems is given in Table 3. Computation time for the complete multi-objective problem is approximately the number of Pareto-optimal points for a given curve in Fig. 13, multiplied by the average computation time for each interior-point (IP) solution reported in Table 3.

To compare the computational cost across the range of spline design resolutions, Table 3 lists the cost per single IP run (i.e., the time to find one point in the Pareto set). The computation time required to calculate both objective functions for a single design was typically less than 0.1 seconds. The solution time for a single IP run, however, increases significantly with N. For higher-resolution cases (e.g., N=5,6,7), functional performance increases as shown in Fig. 13, but this must be weighed against the increase in computational expense quantified in Table 3. An

appropriate choice may depend on a number of factors, including application and whether the studies are supporting early- or late-stage design decisions.

6.6 A remark on boundary conditions

The Reynolds equation derived for this study predicts the pressure field with assumptions that recirculation is not present in the velocity field, that the r and θ direction velocity field is a linear combination of simple shear and pressure driven flow, that the outermost boundary does not experience any shear stress, and that the pressure at the outer boundary is at atmospheric pressure. It is not possible, however, to define these assumptions in the boundary conditions explicitly because the Reynolds equation only defines and manipulates the pressure field (unlike the Navier-Stokes equation). This limitation of Reynolds equation at times may produce results that are not physically meaningful.

In the design studies presented here it is assumed that texture variations extend all the way to the outermost boundary of the sector. Imposing that the pressure is a constant at the outer edge with the texture varying at the outer edge, however, eliminates the pressure driven flow term in the θ direction that would otherwise be non-zero. This would cause the r component of velocity to be non-zero by mass conservation at the outer edge, resulting in a non-zero shear stress at the outer boundary. As a result, the normal force predicted by the Reynolds equation simulation has an sign opposite to behavior predicted by Navier-Stokes solutions. Resolving this modeling issue is a topic of ongoing work. One promising strategy that allows continued use of computationally efficient Reynolds equation solution, while correcting for the above issue, is to expand the modeling domain radially beyond the texture design domain. Initial studies have shown that adding a small annular flat region beyond the maximum radius for texture design produces results that are much closer to Navier-Stokes solution. Another possible strategy is to constrain the gradient of the pressure in the r direction at the outermost boundary of the sector to be zero. This can be derived using continuity of normal stress at a lubricant-air interface, and imposes a no-penetration condition on the lubricant velocity, meaning that the fluid inside the texture is never flung out.

7 CONCLUSION

Full-film lubrication problems have been studied extensively in the tribology community, often with the objective of improving fluid power system efficiency. Using textured contact surfaces in fluid power systems is known to be effective for reducing frictional energy loss. More recently, an experimental study has revealed that asymmetric texture patterns can improve performance further by generating net normal forces to carry higher loads. Based on these previous discoveries pertaining to full-film lubrication, this article presented an investigation of how the transition to more sophisticated texture designs can im-

prove performance in exceptional ways, and has offered insights into the underlying mechanisms that enable these improvements. The studies presented here focused on simultaneous improvement of apparent viscosity and normal force. Predefined texture shapes, such as cylindrical dimples, limit potential performance improvements through contact surface texture design. A general design pattern was clearly present among the Pareto-optimal results for the asymmetric spline-based design study. The resulting designs resemble a helical blade, and observations of the flow and pressure fields provide insight into the mechanisms leveraged by these designs to improve performance.

The ultimate objective of these and other related efforts is to realize new levels of performance and efficiency for fluid power systems, and to reveal physical and design principles that support these improvements. Ongoing efforts complement the results presented here, including development of new models and solution techniques that will enable computationally-efficient design of very high resolution texture geometries by capitalizing on problem structure. Next steps include investigation of full-film lubrication problems in configurations that are more representative of practical fluid power systems, investigating texture design representations based on generative algorithms, incorporating manufacturability and cost considerations, and transitioning from Newtonian to non-Newtonian fluid system models. Optimization results have provided a rich set of design data from which qualitative design insights can be extracted. Future work will iteratively deepen, validate, and enhance this qualitative understanding, leading to valuable design knowledge that may impact fluid power system design practice.

8 ACKNOWLEDGEMENTS

REFERENCES

[1] Wakuda, M., Yamauchi, Y., Kanzaki, S., and Yasuda, Y., 2003. "Effect of surface texturing on friction reduction between ceramic and steel materials under lubricated sliding contact". *Wear, 254*(3-4), pp. 356–363.

[2] Johnston, M. T., King, W. P., and Ewoldt, R. H., 2015. "Shear stress characteristics of microtextured surfaces in gap-controlled hydrodynamic lubrication". *Tribology International, 82*, pp. 123–132.

[3] Rao, L. G., Schuh, J. K., Ewoldt, R. H., and Allison, J. T., 2015. "On Using Adaptive Surrogate Modeling in Design for Efficient Fluid Power". In ASME 2015 International Design Engineering Technical Conferences and Computers and Information in Engineering Conference, ASME.

[4] Burton, R. A., 1963. "Effects of Two-Dimensional, Sinusoidal Roughness on the Load Support Characteristics of a Lubricant Film". *Journal of Fluids Engineering, 85*(2), pp. 258–262.

[5] Tzeng, S. T., and Saibel, E., 1967. "Surface Roughness Effect on Slider Bearing Lubrication". *ASLE Transactions, 10*(3), pp. 334–348.

[6] Lipson, H., 2012. "Frontiers in additive manufacturing". *The Bridge, 42*(1), pp. 5–12.

[7] Hao, X., Pei, S., Wang, L., Xu, H., He, N., and Lu, B., 2014. "Microtexture fabrication on cylindrical metallic surfaces and its application to a rotor-bearing system". *The International Journal of Advanced Manufacturing Technology, 78*(5-8), pp. 1021–1029.

[8] Arghir, M., Roucou, N., Helene, M., and Frene, J., 2003. "Theoretical Analysis of the Incompressible Laminar Flow in a Macro-Roughness Cell". *Journal of Tribology, 125*(2), pp. 309–318.

[9] Stachowiak, G. W., and Batchelor, A. W., 1993. *Engineering Tribology*. Elsevier, Amsterdam.

[10] Schuh, J. K., 2015. "Surface textures and non-Newtonian fluids for decreased friction in full film lubrication". Master's thesis, University of Illinois at Urbana-Champaign, Urbana, IL.

[11] Samareh, J. A., 2001. "Survey of Shape Parameterization Techniques for High-Fidelity Multidisciplinary Shape Optimization". *AIAA Journal, 39*(5), pp. 877–884.

[12] Schuh, J. K., and Ewoldt, R. H., 2016. "Asymmetric surface textures decrease friction with Newtonian fluids in full film lubricated sliding contact". *Tribology International, 97*, pp. 490–498.

[13] Sawaragi, Y., Nakayama, H., and Tanino, T., 1985. "Solution Concepts and Some Properties of Solutions". In *Theory of Multiobjective Optimization*. Academic Press, Orlando, pp. 32–91.

[14] Deb, K., 1999. "Multi-objective Genetic Algorithms: Problem Difficulties and Construction of Test Problems". *Evolutionary Computation, 7*(3), pp. 205–230.

[15] Ehrgott, M., 2005. "Scalarization Techniques". In *Multicriteria Optimization*. Springer-Verlag, Berlin/Heidelberg.

[16] Haimes, Y. Y., Lasdon, L. S., and Wismer, D. A., 1971. "On a Bicriterion Formulation of the Problems of Integrated System Identification and System Optimization". *IEEE Transactions on Systems, Man, and Cybernetics, SMC-1*(3), pp. 296–297.

[17] Bauer, W., 2011. *Hydropneumatic suspension systems*. Springer, Heidelberg.

[18] Heath, M. T., 2002. *Scientific Computing: An Introductory Survey*, 2 ed. McGraw-Hill.

[19] Fornberg, B., 2009. *A practical guide to pseudospectral methods*. Cambridge University Press, Cambridge.